Available online at www.sciencedirect.com
SCIENCE DIRECT®
Journal of Computational Physics 211 (2006) 154–178
JOURNAL OF COMPUTATIONAL PHYSICS
www.elsevier.com/locate/jcp

Extension of the spectral volume method to high-order boundary representation

Z.J. Wang [a,*], Yen Liu [b,1]

[a] Department of Aerospace Engineering, College of Engineering, Iowa State University, 2271 Howe Hall, Ames, IA 50011, USA
[b] NASA Ames Research Center, Mail Stop T27B-1, Moffett Field, CA 94035, USA

Received 5 August 2004; received in revised form 10 May 2005; accepted 18 May 2005
Available online 20 July 2005

Abstract

In this paper, the spectral volume method is extended to the two-dimensional Euler equations with curved boundaries. It is well-known that high-order methods can achieve higher accuracy on coarser meshes than low-order methods. In order to realize the advantage of the high-order spectral volume method over the low order finite volume method, it is critical that solid wall boundaries be represented with high-order polynomials compatible with the order of the interpolation for the state variables. Otherwise, numerical errors generated by the low-order boundary representation may overwhelm any potential accuracy gains offered by high-order methods. Therefore, more general types of spectral volumes (or elements) with curved edges are used near solid walls to approximate the boundaries with high fidelity. The importance of this high-order boundary representation is demonstrated with several well-know inviscid flow test cases, and through comparisons with a second-order finite volume method.

Keywords: High order; Finite volume; Unstructured grids; Spectral volume; Boundary condition

1. Introduction

The spectral volume (SV) method is a recently developed high-order finite volume (FV) method for hyperbolic conservation laws on unstructured grids [16–19]. The SV method belongs to a general class of Godunov-type finite volume method [8,14], which has been under development for several decades, and has become the state-of-the-art for the numerical solution of hyperbolic conservation laws. For a more detailed

* Corresponding author. Tel.: +515 294 1614; fax: +515 294 3262.
E-mail addresses: zjw@iastate.edu (Z.J. Wang), liu@nas.nasa.gov (Y. Liu).
[1] Tel.: 650 604 6667.

0021-9991/$ - see front matter
doi:10.1016/j.jcp.2005.05.022

review of the literature on the Godunov-type method, refer to [16], and the references therein. Some widely used numerical methods for conservation laws such as the k-exact finite volume [2], the essentially non-oscillatory (ENO) [9,1], and weighted ENO [10] methods are also Godunov-type methods. The SV method is also related to a popular finite-element method for hyperbolic conservation laws, the discontinuous Galerkin (DG) method [6,7,3] in that multiple degrees of freedom are used in a single element. Similar to the Godunov method, the SV method has two key ingredients. One is the solution reconstruction, and the other is the (approximate) Riemann solver. What distinguishes the SV method from the k-exact FV method [2] is the solution reconstruction. Instead of using a (large) stencil of neighboring cells to perform a high-order polynomial reconstruction, a simplex unstructured grid cell – called a spectral volume – is partitioned into a "structured" set of sub-cells called control volumes (CVs), and cell-averaged state variables on these sub-cells are then the degrees-of-freedom (DOFs), which are used to perform high-order polynomial reconstructions for the state variables inside the SV. Several convergent partitions of a triangle are presented in [17,11] and shown in Fig. 1. If all SVs are partitioned in a geometrically similar manner, a universal reconstruction is obtained for all simplexes. Recently the SV method has been successfully demonstrated for 2D Euler equations with both smooth features and discontinuities [19], and extended to three dimensions [11].

The main advantage of high-order numerical methods (order >2) over low order ones (order $\leqslant 2$) is its efficiency in attaining a given level of accuracy. In other words, high-order methods can potentially achieve a higher-level of accuracy than low order ones given the same computational resources. This advantage of the SV method over a second-order MUSCL-type FV method [14] has been demonstrated in [19] with an accuracy study. In making comparisons between the FV and SV methods, it should be noted that the SV method introduces more unknowns in a computational element or a grid cell. It is unfair to the FV method

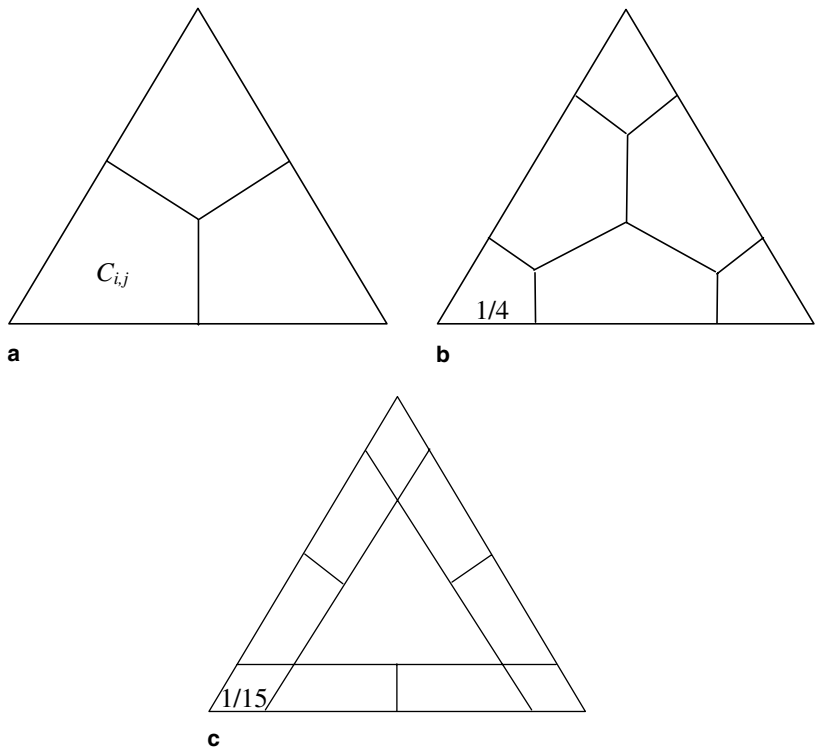

Fig. 1. Partitions of various orders in a triangular spectral volume. (a) Linear. (b) Quadratic. (c) Cubic.

if one simply compares the solution accuracy on a given computational grid since the SV method employs many times more unknowns on the same grid. A much fairer evaluation is to compare the solution accuracy of a SV and FV scheme with the same number of unknowns. Therefore, the computational grid for the SV method should be much coarser than that for the FV method. In fact, many such comparisons have been made in [19], and it has been found that a fourth-order SV scheme is capable of producing much more accurate solutions on much coarser meshes than a second-order FV scheme. If a grid is fine enough for a second-order FV scheme to produce accurate results, this grid is then too fine for a fourth-order SV scheme. In generating coarse meshes for high-order SV schemes, it is critical that curved boundaries are represented with high fidelity. Otherwise, the error produced by a low-fidelity representation of a curved boundary may render the solution accuracy to first or second-order, essentially making the high-order schemes low order. The importance of high-order boundary representation for the high-order DG method has been demonstrated in [3].

The paper is organized as follows. In Section 2, the SV method for the Euler equations is briefly reviewed. In Section 3, the extension of the SV method to more general elements with curved edges is described. Several high-order elements with a single curved side are presented, and implemented for the Euler solver. Three inviscid flow problems including the flow over a cylinder, the Ringleb flow and a subsonic flow over a NACA0012 airfoil are presented in Section 4. The numerical orders of accuracy for these cases are computed based on grid refinement studies, and a second-order FV method is again compared with a fourth-order SV method. Finally conclusions from the present study are presented in Section 5.

2. Spectral volume method for the 2D Euler equations

The two-dimensional, unsteady Euler equations in conservative form can be written as

$$\frac{\partial Q}{\partial t}+\frac{\partial E}{\partial x}+\frac{\partial F}{\partial y}=0, \tag{2.1a}$$

where Q is the vector of conserved variables, E and F are the inviscid flux vectors given below:

$$Q=\begin{Bmatrix}\rho\\ \rho u\\ \rho v\\ E_t\end{Bmatrix},\quad E=\begin{Bmatrix}\rho u\\ \rho u^2+p\\ \rho uv\\ u(E_t+p)\end{Bmatrix},\quad F=\begin{Bmatrix}\rho v\\ \rho uv\\ \rho v^2+p\\ v(E_t+p)\end{Bmatrix}. \tag{2.1b}$$

Here ρ is the density, u and v are the velocity components in x and y directions, p is the pressure, and E_t is the total energy. The pressure is related to the total energy by

$$E_t=\frac{p}{\gamma-1}+\frac{1}{2}\rho(u^2+v^2) \tag{2.1c}$$

with a constant ratio of specific heats γ. In all test cases in the present study, γ is taken to be 1.4 for air. Assume that (2.1) is solved in a computational domain Ω subject to proper initial and boundary conditions. The domain Ω is discretized into N non-overlapping triangular elements called spectral volumes (SVs)

$$\Omega=\bigcup_{i=1}^{N}S_i. \tag{2.2}$$

Given a desired order of accuracy k for (2.1), each spectral volume S_i is then partitioned into $m = k(k + 1)/2$ control volumes (CVs), and the jth CV of S_i is then denoted by $C_{i,j}$. The cell-averaged conservative variable Q at time t for control volume $C_{i,j}$ is defined as

$$\bar{Q}_{i,j}(t) = \frac{\int_{C_{i,j}} Q(x,y,t)\,\mathrm{d}x\,\mathrm{d}y}{V_{i,j}}, \quad j = 1,\ldots,m, \;\; i = 1,\ldots,N, \tag{2.3}$$

where $V_{i,j}$ is the volume of $C_{i,j}$. Given the cell-averaged conservative variables for all the CVs in S_i, a polynomial $p_i(x,y) \in P^{k-1}$ (the space of polynomials of degree at most $k-1$) can be reconstructed such that it is a kth order accurate approximation to $Q(x,y)$ inside S_i:

$$p_i(x,y) = Q(x,y) + \mathrm{O}(h^k), \quad (x,y) \in S_i, \;\; i = 1,\ldots,N. \tag{2.4}$$

This reconstruction can be solved analytically by satisfying the following conditions:

$$\frac{\int_{C_{i,j}} p_i(x,y)\,\mathrm{d}x\,\mathrm{d}y}{V_{i,j}} = \bar{Q}_{i,j}, \quad j = 1,\ldots,m. \tag{2.5}$$

This polynomial $p_i(x,y)$ is the kth order approximation we are looking for as long as the solution $Q(x,y)$ is smooth in the region covered by S_i. The reconstruction can be more conveniently expressed as

$$p_i(x,y) = \sum_{j=1}^{m} L_j(x,y)\bar{Q}_{i,j}, \tag{2.6}$$

where $L_j(x,y) \in P^{k-1}$ are the "shape" functions which satisfy

$$\frac{\int_{C_{i,j}} L_m(x,y)\,\mathrm{d}x\,\mathrm{d}y}{V_{i,j}} = \delta_{jm}. \tag{2.7}$$

The high-order reconstruction is then used to generate high-order updates for the cell-averaged state variable on the CVs using the usual finite volume method with proper quadrature formulas. Integrating (2.1) in a general CV such as the one shown in Fig. 1, we obtain

$$\frac{\mathrm{d}\bar{Q}_{i,j}}{\mathrm{d}t} + \frac{1}{V_{i,j}} \sum_{r=1}^{K} \int_{A_r} (\mathbf{f}\cdot\mathbf{n})\,\mathrm{d}A = 0, \tag{2.8}$$

where $\mathbf{f} = (E,F)$, K is the number of faces in $C_{i,j}$ and A_r represents the rth face of $C_{i,j}$. The surface integral on each face can be performed with a kth order accurate Gauss quadrature formula, i.e.

$$\int_{A_r} (\mathbf{f}\cdot\boldsymbol{n})\,\mathrm{d}A \approx \sum_{q=1}^{J} w_{rq}\mathbf{f}(Q(x_{rq},y_{rq}))\cdot\boldsymbol{n}_{rq}A_r, \tag{2.9}$$

where $J = \text{integer}[(k+1)/2]$ is the number of quadrature points on the rth face, w_{rq} are the Gauss quadrature weights, (x_{rq}, y_{rq}) are the Gauss quadrature points. The normal component of the flux vector is replaced with a Riemann flux [12] given the reconstructed left and right state variables, i.e.

$$\mathbf{f}\cdot\boldsymbol{n} \approx \hat{f}(Q_{\mathrm{L}}, Q_{\mathrm{R}}, \boldsymbol{n}). \tag{2.10}$$

Note that the Riemann flux is only used on interfaces between neighboring SVs. The analytical physical flux is used on internal interfaces belonging to the same SV. The Riemann flux also provides the proper characteristic coupling between neighboring SVs. For time integration, we use the third-order TVD Runge-Kutta scheme from [13]. Other details of the method can be found in [19].

3. High-order spectral volumes with curved boundary

An advantage of any high-order methods is that fewer number of unknowns are required to achieve a given level of accuracy than with lower order methods. Therefore the computational grids used in high-or-

der simulations may be considered coarse comparing with those in second-order simulations. In second-order CFD simulations, all curved boundaries are represented with line-segments or planar facets since the representation is compatible with the linear data interpolations used in second-order flow solvers. In order to minimize the solution errors produced by this "crude" approximation of curved boundaries, many elements may be required to just preserve the geometry with a reasonable precision. If this crude geometric representation is used in high-order simulations, unnecessarily fine grids may be required near curved boundaries to represent the boundary with high fidelity. Obviously this practice can waste significant computational resources. A much more desirable approach is to represent curved boundaries with higher order polynomials compatible with the order of the data reconstruction. For example, quadratic or cubic polynomials should be used to approximate boundaries in third and fourth-order SV schemes, which employ quadratic and cubic polynomials to represent the solution variables. Following the usual practice in high-order finite element method [20], isoparametric SVs can be used to map SVs with curved boundaries into the standard SV. Assume that a one-to-one transformation exists between a general SV in the physical space (x, y) and the standard triangle in the computational domain (ξ, η) as shown in Fig. 2, i.e.,

$$\begin{aligned} \xi &= \xi(x, y), \\ \eta &= \eta(x, y). \end{aligned} \tag{3.1}$$

The partition of the SV is performed in the standard triangle, and the partition in the physical domain is the result of the inverse transformation from the computational domain back to the physical domain as shown in Fig. 3

$$\begin{aligned} x &= x(\xi, \eta), \\ y &= y(\xi, \eta). \end{aligned} \tag{3.2}$$

Therefore a necessary condition for a valid transformation is that the inverse transformation exists. The DOFs for the general SV are the CV-averaged state variables in the physical domain, i.e.

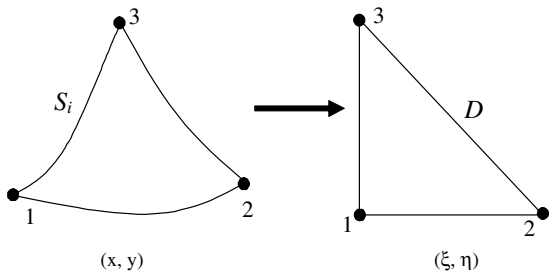

Fig. 2. Transformation of a general SV in the physical domain to the standard triangle in the computational domain.

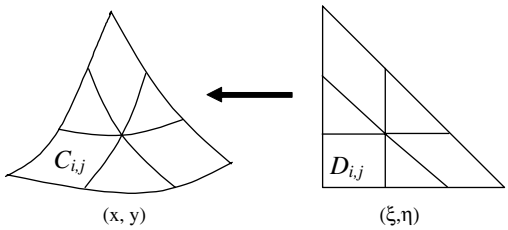

Fig. 3. Transformation of the partition from the standard triangle in the computational domain to the general SV in the physical domain.

$$\bar{Q}_{i,j} = \frac{\int_{C_{i,j}} Q(x,y)\,\mathrm{d}x\,\mathrm{d}y}{\int_{C_{i,j}} \mathrm{d}x\,\mathrm{d}y} = \frac{\int_D Q(\xi,\eta)|J|\,\mathrm{d}\xi\,\mathrm{d}\eta}{\int_D |J|\,\mathrm{d}\xi\,\mathrm{d}\eta}, \tag{3.3}$$

where J is the Jacobian matrix of the transformation, i.e., $J = \frac{\partial(x,y)}{\partial(\xi,\eta)}$. The reconstruction problem then reads: given the CV-averaged state-variables in all the CVs of a SV, reconstruct a degree $k-1$ polynomial $p_i(\xi,\eta)$ in the computational domain such that

$$\int_D p_i(\xi,\eta)|J|\,\mathrm{d}\xi\,\mathrm{d}\eta = \bar{Q}_{i,j}\int_D |J|\,\mathrm{d}\xi\,\mathrm{d}\eta. \tag{3.4}$$

Given a basis set and a valid transformation, the reconstruction problem can be solved either analytically or numerically to obtain the reconstruction coefficients. However, different curved SVs have different reconstruction coefficients. Therefore it is necessary to store these coefficients for SVs with curved boundaries. Since the number of curved SVs is expected to be small compared with the total number of SVs in any simulation, the cost of storing these coefficients should be small.

In the most general case, a quadratic isoparametric SV requires the specification of 6 nodes, while a cubic SV requires the specification of 10 nodes, as shown in Fig. 4. Then the transformation can be expressed as

$$\mathbf{r} = \sum_{j=1}^{m} M_j(\xi,\eta)\mathbf{r}_j, \tag{3.5}$$

where $\mathbf{r} = (x,y)$. The shape functions for a quadratic SV can be written as

$$\begin{aligned} M_1(\xi,\eta) &= (1-\xi-\eta)(1-2\xi-2\eta),\\ M_2(\xi,\eta) &= \xi(2\xi-1),\\ M_3(\xi,\eta) &= \eta(2\eta-1),\\ M_4(\xi,\eta) &= 4\xi\eta,\\ M_5(\xi,\eta) &= 4\xi(1-\xi-\eta),\\ M_6(\xi,\eta) &= 4\eta(1-\xi-\eta). \end{aligned} \tag{3.6}$$

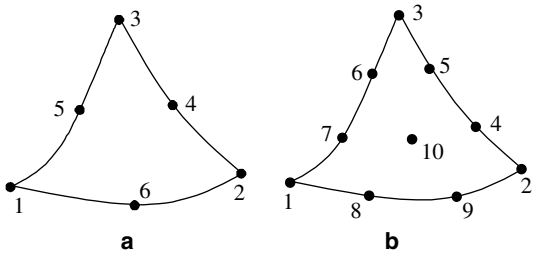

Fig. 4. Quadratic and cubic isoparametric SVs.

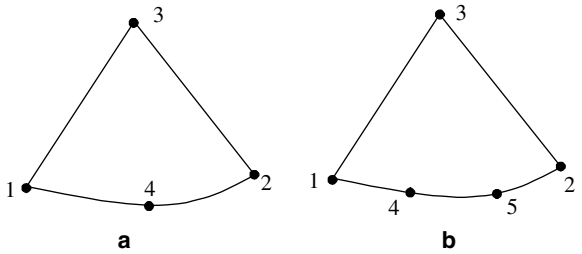

Fig. 5. Simplified quadratic and cubic SVs with one curved boundary.

In the cases we have computed so far, it is not necessary to use the most general isoparametric SV since only one boundary of the SV is usually curved as shown in Fig. 5. As a result, simplified curved SVs (SCSV) can be used. For example, only four or five nodes are required to determine uniquely a quadratic or a cubic SCSV, which has one curved side represented by quadratic or cubic polynomials, dramatically simplifying the process of specifying these SVs and the derivation of the reconstruction coefficients. The shape functions for the quadratic SCSV can be easily found to be

$$\begin{aligned} M_1(\xi,\eta) &= 1 - 3\xi + 2\xi(\xi+\eta) - \eta, \\ M_2(\xi,\eta) &= -\xi + 2\xi(\xi+\eta), \\ M_3(\xi,\eta) &= \eta, \\ M_4(\xi,\eta) &= 4\xi(1-\xi-\eta). \end{aligned} \tag{3.7}$$

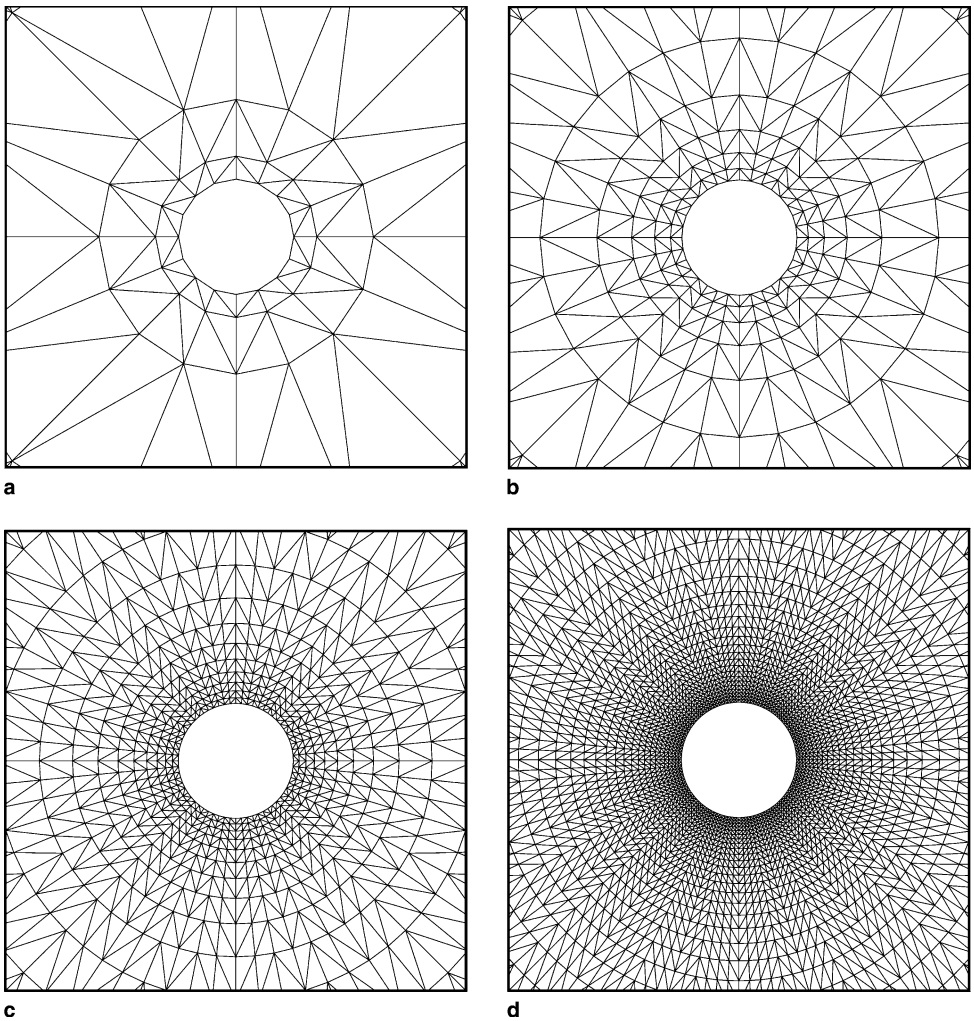

Fig. 6. Computational grids for flow over a circular cylinder. (a) $16\times4\times2$ mesh. (b) $32\times8\times2$mesh. (c) $64\times16\times2$ mesh. (d) $128\times32\times2$ mesh.

The shape functions for the cubic SCSV are

$$\begin{aligned} M_1(\xi,\eta) &= 1 - 5.5\xi - \eta + 9\xi(\xi+\eta) - 4.5\xi(\xi+\eta)^2, \\ M_2(\xi,\eta) &= \xi[1 - 4.5(\xi+\eta) + 4.5(\xi+\eta)^2], \\ M_3(\xi,\eta) &= \eta, \\ M_4(\xi,\eta) &= 9\xi[1 - 2.5(\xi+\eta) + 1.5(\xi+\eta)^2], \\ M_5(\xi,\eta) &= \xi[-4.5 + 18(\xi+\eta) - 13.5(\xi+\eta)^2]. \end{aligned} \tag{3.8}$$

The surface integral in the physical domain (2.8) is also transformed to a surface integral in the computational domain. Let the equation of the rth face of C_{ij} in the standard SV be

$$\eta = \eta_r(\xi), \quad \xi_{r1} < \xi < \xi_{r2}. \tag{3.9}$$

Then obviously along the face

$$\mathrm{d}\eta = \eta_r' \mathrm{d}\xi \tag{3.10}$$

and

$$\begin{aligned} \mathrm{d}x &= \frac{\partial x}{\partial \xi}\mathrm{d}\xi + \frac{\partial x}{\partial \eta}\mathrm{d}\eta = \left(\frac{\partial x}{\partial \xi} + \frac{\partial x}{\partial \eta}\eta_r'\right)\mathrm{d}\xi, \\ \mathrm{d}y &= \frac{\partial y}{\partial \xi}\mathrm{d}\xi + \frac{\partial y}{\partial \eta}\mathrm{d}\eta = \left(\frac{\partial y}{\partial \xi} + \frac{\partial y}{\partial \eta}\eta_r'\right)\mathrm{d}\xi, \\ \mathrm{d}A &= \left(\mathrm{d}x^2 + \mathrm{d}y^2\right)^{1/2} = \left(\left(\frac{\mathrm{d}x}{\mathrm{d}\xi}\right)^2 + \left(\frac{\mathrm{d}y}{\mathrm{d}\xi}\right)^2\right)^{1/2}\mathrm{d}\xi, \end{aligned} \tag{3.11}$$

Table 1
Accuracy study of SV schemes with subsonic flow around a circular cylinder

Order of interpolation	Grid	L_∞ error	L_∞ order	L_1 error	L_1 order
I1B1 (nq = 1)	$16\times4\times2$	2.68e − 2	–	3.66e − 3	–
	$32\times8\times2$	1.43e − 2	0.91	1.07e − 3	1.77
	$64\times16\times2$	6.98e − 3	1.03	2.92e − 4	1.87
	$128\times32\times2$	3.98e − 3	0.81	8.07e − 5	1.86
I2B2 (nq = 2)	$16\times4\times2$	3.18e − 3	–	1.54e − 4	–
	$32\times8\times2$	4.73e − 4	2.75	2.45e − 5	2.65
	$64\times16\times2$	1.38e − 4	1.78	3.82e − 6	2.68
	$128\times32\times2$	3.03e − 5	2.19	4.94e − 7	2.95
I3B3 (nq = 2)	$16\times4\times2$	4.15e − 4	–	4.88e − 5	–
	$32\times8\times2$	3.64e − 5	3.51	3.06e − 6	4.00
	$64\times16\times2$	4.56e − 6	3.00	2.69e − 7	3.51
	$128\times32\times2$	7.60e − 7	2.58	2.29e − 8	3.55
I3B3 (nq = 3)	$16\times4\times2$	4.99e − 4	–	4.71e − 5	–
	$32\times8\times2$	3.70e − 5	3.75	2.90e − 6	4.02
	$64\times16\times2$	4.72e − 6	2.97	2.56e − 7	3.50
	$128\times32\times2$	8.28e − 7	2.51	2.30e − 8	3.48
I3B2 (nq = 2)	$16\times4\times2$	9.17e − 4	–	4.04e − 5	–
	$32\times8\times2$	3.71e − 5	4.63	3.65e − 6	3.47
	$64\times16\times2$	5.84e − 6	2.67	3.48e − 7	3.39
	$128\times32\times2$	1.04e − 6	2.49	3.10e − 8	3.49

where

$$\frac{\mathrm{d}x}{\mathrm{d}\xi} = \frac{\partial x}{\partial \xi} + \frac{\partial x}{\partial \eta}\eta_r',$$
$$\frac{\mathrm{d}y}{\mathrm{d}\xi} = \frac{\partial y}{\partial \xi} + \frac{\partial y}{\partial \eta}\eta_r'.$$

Let the unit outgoing normal of the face be $\boldsymbol{n} = (n_x, n_y)$. Then

$$n_x = \frac{\mathrm{d}y}{\mathrm{d}A}, \qquad n_y = -\frac{\mathrm{d}x}{\mathrm{d}A}. \tag{3.12}$$

The surface integral in (2.8) becomes

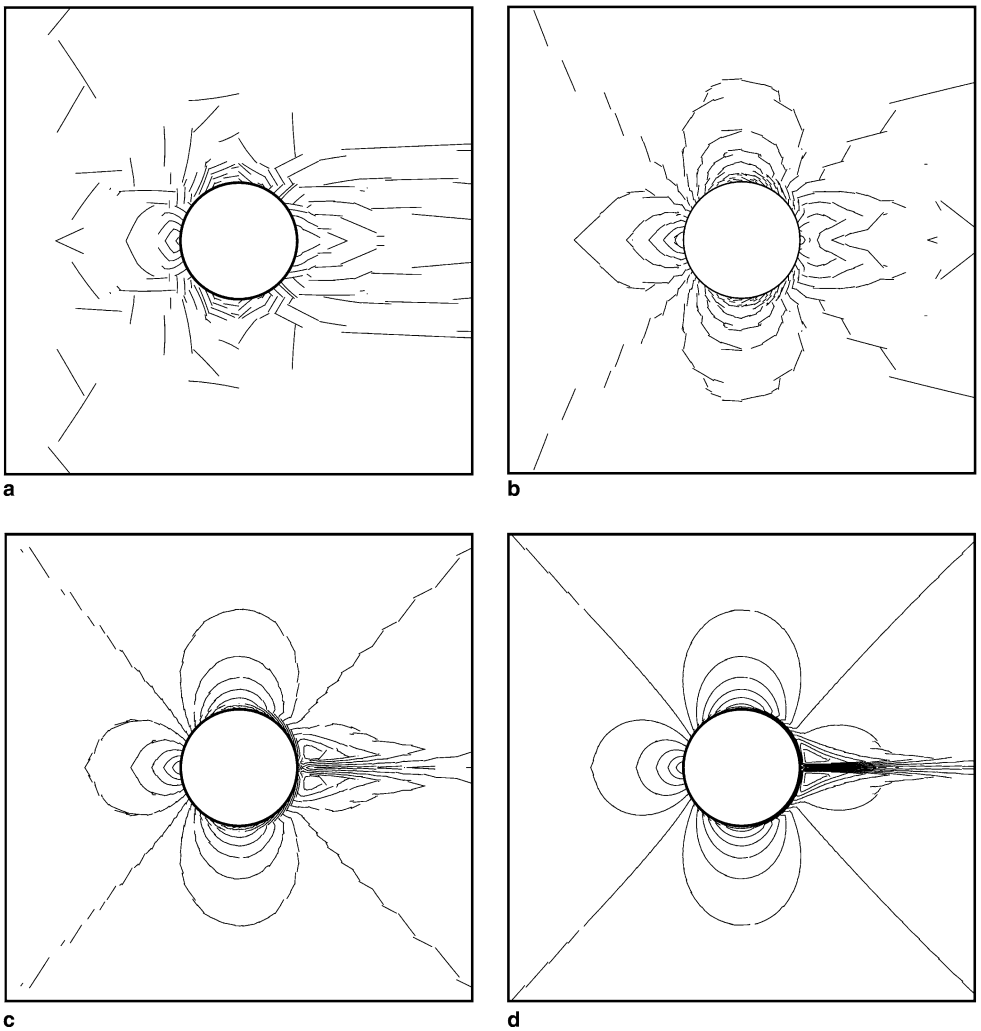

Fig. 7. Mach contours computed with I1B1 spectral volumes.

$$\int_{A_r} (\mathbf{f}\cdot\boldsymbol{n})\,\mathrm{d}A = \int_{A_r} \mathbf{f}\cdot\left(\frac{\mathrm{d}y}{\mathrm{d}A}, -\frac{\mathrm{d}x}{\mathrm{d}A}\right)\mathrm{d}A = \int_{\xi_{r1}}^{\xi_{r2}} \mathbf{f}\cdot\left(\frac{\mathrm{d}y}{\mathrm{d}\xi}, -\frac{\mathrm{d}x}{\mathrm{d}\xi}\right)\mathrm{d}\xi. \tag{3.13}$$

This line integral in the standard element can be evaluated using the standard Gaussian quadrature formula

$$\int_{\xi_{r1}}^{\xi_{r2}} \mathbf{f}\cdot\left(\frac{\mathrm{d}y}{\mathrm{d}\xi}, -\frac{\mathrm{d}x}{\mathrm{d}\xi}\right)\mathrm{d}\xi = (\xi_{r2}-\xi_{r1})\sum_{q=1}^{J} w_{rq} f_n(\xi_{rq}), \tag{3.14}$$

where w_{rq} represent the Gauss quadrature weights, and $f_n = \mathbf{f}\cdot\left(\frac{\mathrm{d}y}{\mathrm{d}\xi}, -\frac{\mathrm{d}x}{\mathrm{d}\xi}\right)$. To preserve a uniform free stream (Q = constant), the surface integral must satisfy the following identity

$$\sum_{r=1}^{K}\int_{A_r} \boldsymbol{n}\,\mathrm{d}A = \int_{A_r}\left(\left(\frac{\partial y}{\partial\xi}+\frac{\partial y}{\partial\eta}\eta_r'\right), -\left(\frac{\partial x}{\partial\xi}+\frac{\partial x}{\partial\eta}\eta_r'\right)\right)\mathrm{d}\xi. \tag{3.15}$$

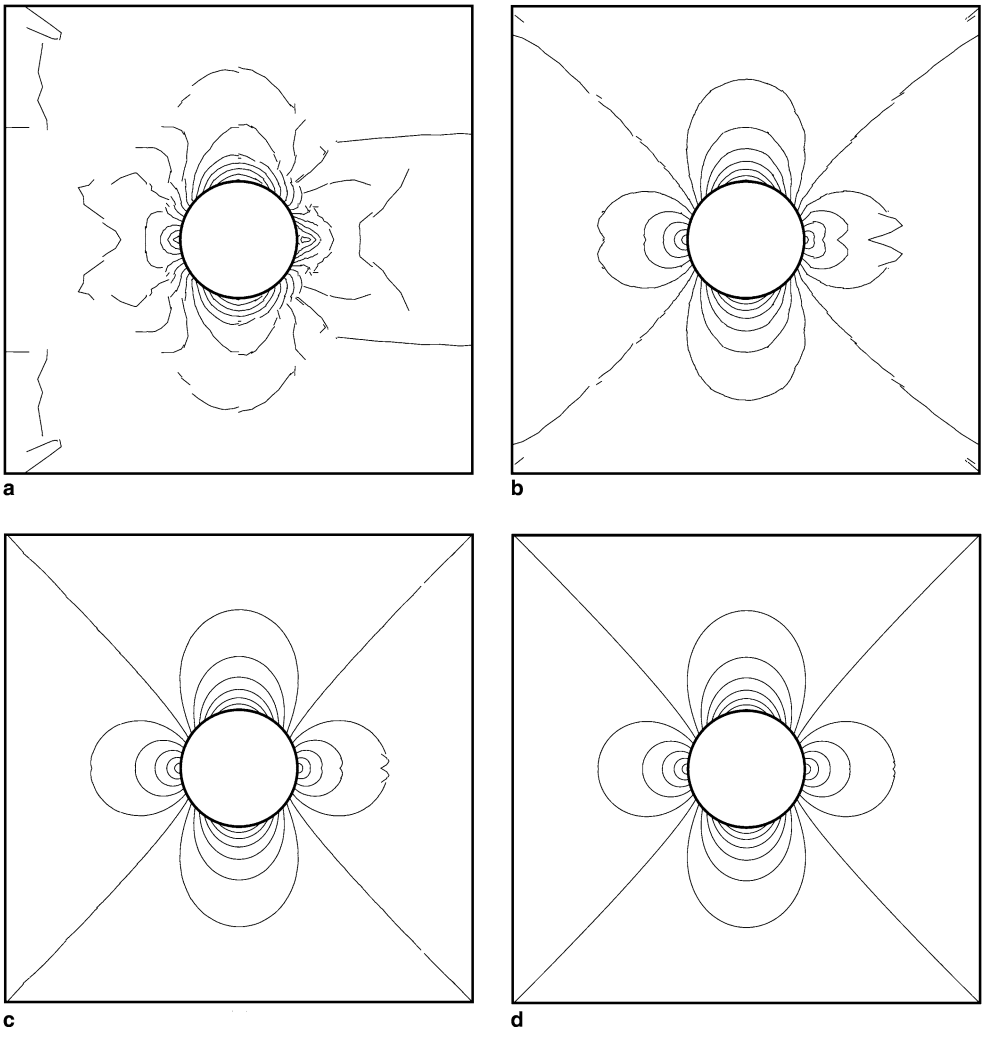

Fig. 8. Mach contours computed with I2B2 spectral volumes.

Since $\eta = \eta_r(\xi)$ is a line-segment in the standard element, η_r' is a constant. It is obvious that (n_x, n_y) are polynomials one order lower than the transformation polynomials (3.2). Therefore, a one-point Gauss formula is sufficient to preserve a free stream for a quadratic boundary representation, while a two-point Gauss formula is need for a cubic boundary representation. Because a two-point Gauss formula is employed for both quadratic and cubic data reconstructions, free-stream is automatically preserved with third- or fourth-order SV schemes. If the flux function is of the same order of polynomial as the solution, more quadrature points are obviously required to exactly integrate the flux over curved boundaries. In this case, a linear solution with a quadratic boundary representation requires a two point Gauss quadrature formula while a cubic solution with a cubic boundary requires a three point Gauss quadrature formula. In most of the simulations presented in the next section, the number of quadrature points (nq) is 1 for linear, nq is 2 for quadratic and cubic SVs. However, we also will test the performance of the cubic SCSV with nq = 3 for the flow over cylinder.

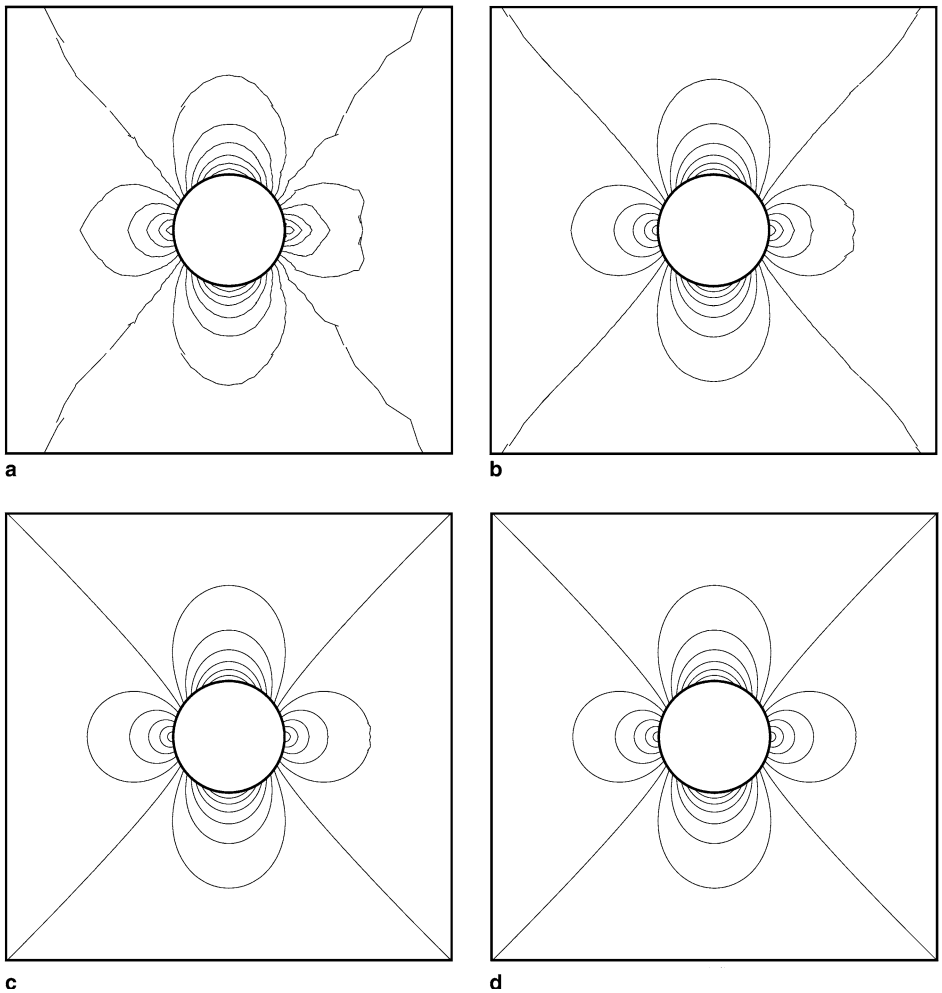

Fig. 9. Mach contours computed with I3B3 spectral volumes.

4. Numerical tests

Several well known inviscid flow problems with curved solid wall boundaries are employed to assess the importance of high-fidelity boundary representation in the SV method. In the case of subsonic flow over a circular cylinder, SV schemes of various orders of accuracy are also evaluated against a second-order FV method [15], which represent the state of the art in commercial CFD software. Both the two-stage and three-stage Runge-Kutta TVD schemes were tested. It was found that the two-stage scheme was slightly more efficient in terms of CPU time for steady state problems. Therefore all the computations were performed with the 2-stage scheme. On a Pentium IV 2.8 GHz machine running Linux, the CPU time per time-step (two Runge-Kutta stages) per SV (or element) is about 18, 47 and 92 μs for linear, quadratic and cubic SVs (all with 2 quadrature points), respectively. The storage requirement is roughly 99, 194 and 361 words for linear, quadratic and cubic SVs. The CFL numbers in terms of the SV are about 1/2, 1/3 and 1/5 for the linear, quadrature and cubic SVs, respectively. The residual used in all convergence histories is the L_1 density residual.

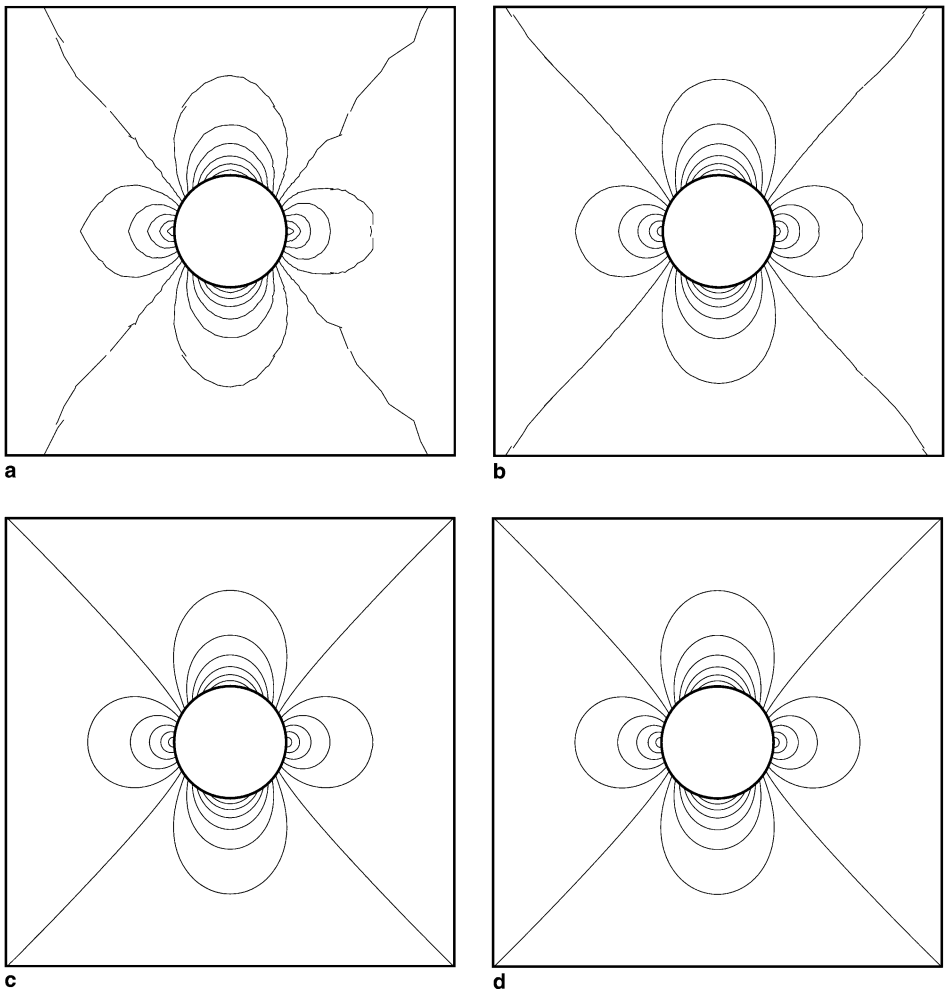

Fig. 10. Mach contours computed with I3B2 spectral volumes.

4.1. Subsonic flow over a circular cylinder

A subsonic inviscid flow around a circular cylinder at Mach = 0.3 is selected to test the new high-order curved SVs. Due to flow symmetry, only the top half of the physical domain is selected as the computational domain although the complete physic domain is displayed in all the figures. The far field boundary is located 20 diameters away from the cylinder center and a characteristic inflow/outflow boundary condition is used in the far field boundary. In order to perform a grid refinement accuracy study, four different triangular grids were generated from four structured grids with 16×4, 32×8, 64×16 and 128×32 cells, which are shown in Fig. 6. Computations on all the grids were started from a uniform free stream, and convergence is declared when the residual is reduced by 10 orders of magnitude. In the first set of tests, the order of the boundary representation is the same as the order of the interior solution representation. In other words, linear-segments are used with linear SVs, quadratic curves are used for quadratic SVs, and cubic curves are employed for cubic SVs. These elements are denoted as I1B1, I2B2 and I3B3 SVs (Interior first-order Boundary first-order, etc.). Since the flow is isentropic, the entropy error in the numerical solution can be used to serve as a very elegant error indicator. The L_1 and L_∞ entropy errors computed on all the grids are presented in Table 1. Note that the designed order accuracy is obtained for all the schemes in the L_1 norm, while there is about an order reduction in the L_∞ norm. The computed Mach number con-

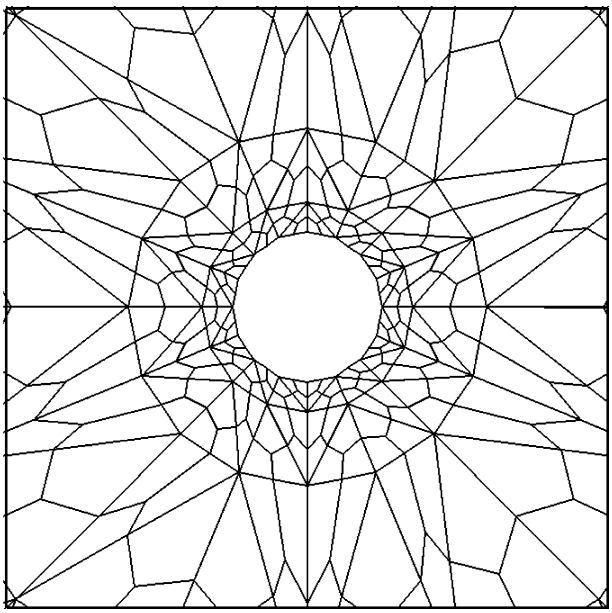

Fig. 11. Coarse control volume grid used for a second-order finite volume scheme.

Table 2
Accuracy study of second-order FV scheme with subsonic flow around a circular cylinder

Order of interpolation	Grid	L_∞ error	L_∞ order	L_1 error	L_1 order
I1B1	$16 \times 4 \times 2 \times 3$	1.40e − 2	–	2.04e − 3	–
	$32 \times 8 \times 2 \times 3$	6.79e − 3	1.04	6.28e − 4	1.70
	$64 \times 16 \times 2 \times 3$	3.12e − 3	1.12	1.76e − 4	1.84
	$128 \times 32 \times 2 \times 3$	1.47e − 3	1.09	5.25e − 5	1.75

tours with all SV schemes are displayed in Figs. 7–9. Obviously, the Mach contours become more and more symmetric with the increase in the order of accuracy and grid resolution. However, a non-symmetric wake structure exists in the second-order SV Mach contours, and it seems this structure does not vanish with grid refinement.

Next we investigate the performance of I3B2 SVs, in which the boundary of a cubic SV is represented with a quadratic representation. The motivation is to study whether it is necessary to approximate curved boundary with higher than quadratic curves. The computed entropy errors using I3B2 SVs are also presented in Table 1 and the computed Mach contours are displayed in Fig. 10. Note that although I3B3 produced slightly more accurate results, the I3B2 elements were capable of achieving nearly fourth-order accuracy in the L_1 norm. This may indicate that a quadratic boundary representation is sufficiently accurate for high-order SV schemes.

In addition, we also tested the performance of I3B3 SVs with three quadrature points on each face (nq = 3). The entropy errors are also presented in Table 1. The results are very similar to those with two quadrature points.

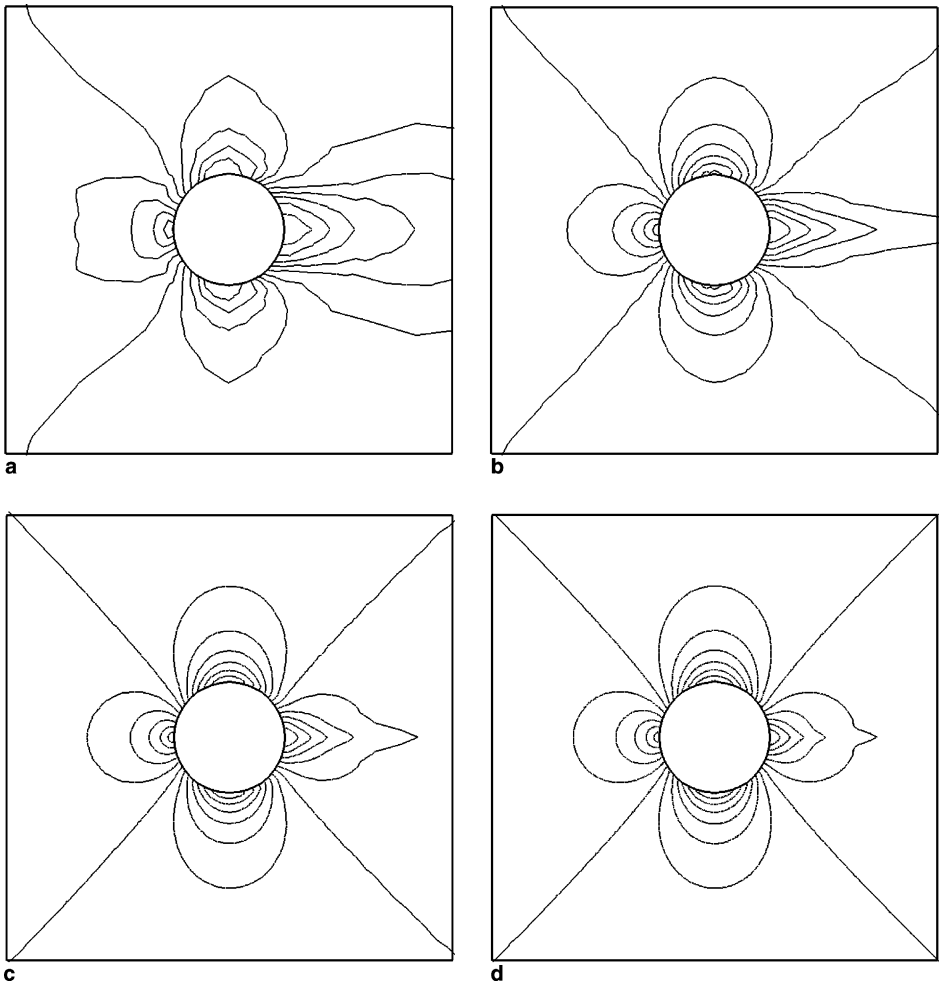

Fig. 12. Mach contours computed with a second-order finite volume method with piece-wise linear boundary representation.

Next a second-order FV method [15] is used to perform the same calculation for comparison purposes. The second-order cell-centered FV scheme uses a least-squares linear reconstruction. As discussed earlier, it is important for both the SV and FV computations to have the same number of DOFs in order to make a fair comparison. Therefore, the computational grids for the FV computations are the same as the subcells (or CVs) of the SVs used in the second-order SV simulations. A sample subcell grid is shown in Fig. 11. The computed entropy errors from the FV method are presented in Table 2, while the Mach contours are shown in Fig. 12. The contours lines are continuous because the solutions are interpolated from cell centers to the nodes, and then averaged. Note that the second-order FV method is able to achieve second-order accuracy in the L_1 norm, but there is also an order reduction in the L_∞ norm. The computed FV solutions have slightly less entropy errors than the SV solutions using the I1B1 element. In addition, the Mach contours with the FV method become more and more symmetric with grid refinement, indicating the second-order FV method is not as sensitive as the second-order SV scheme to the fidelity of the boundary representation. The same phenomenon was also reported by Bassi and Rebay in [3] for the DG method.

In order to test whether a higher order boundary representation makes a difference in a linear SV, an I1B2 SV was implemented. Two quadrature points are required on each face to preserve a linear function

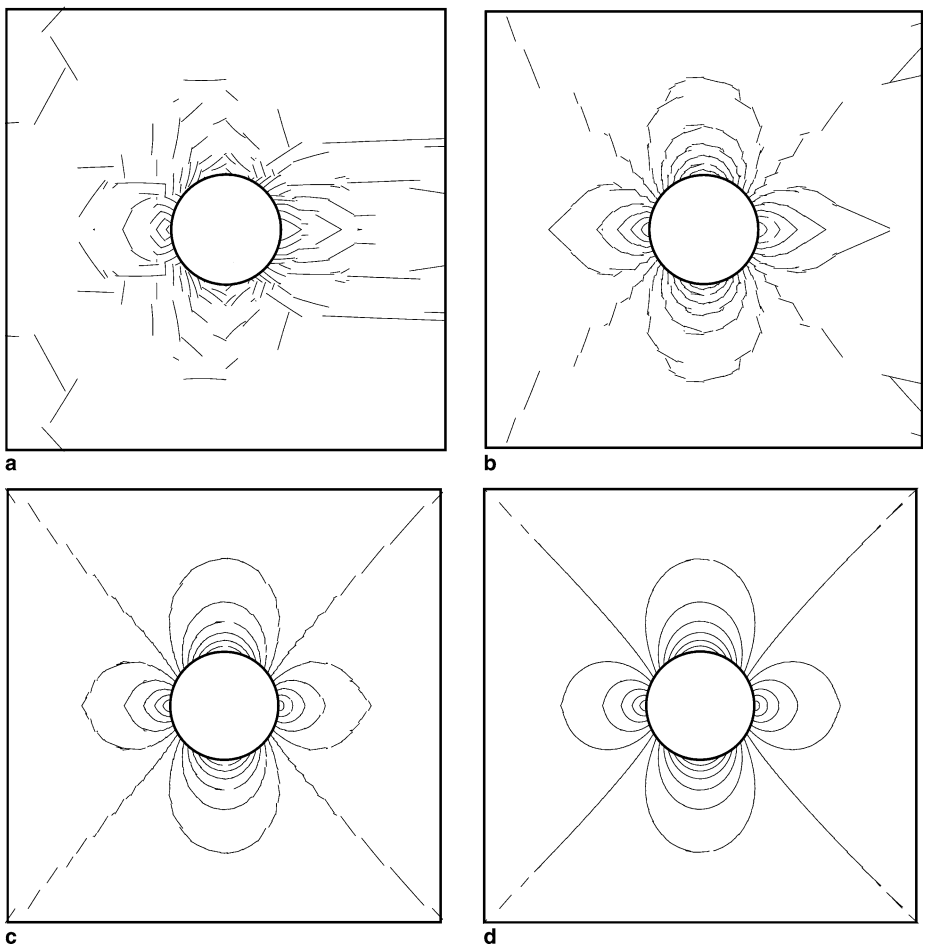

Fig. 13. Mach contours computed with I1B2 spectral volumes.

Table 3
Accuracy study of a second-order SV scheme using quadratic boundary representation with subsonic flow around a circular cylinder

Order of interpolation	Grid	L_∞ error	L_∞ order	L_1 error	L_1 order
I1B2 (nq = 2)	$16\times4\times2$	1.05e − 2	–	1.75e − 3	–
	$32\times8\times2$	3.12e − 3	1.75	3.09e − 4	2.50
	$64\times16\times2$	8.71e − 4	1.84	5.52e − 5	2.48
	$128\times32\times2$	2.11e − 4	2.05	9.92e − 6	2.48

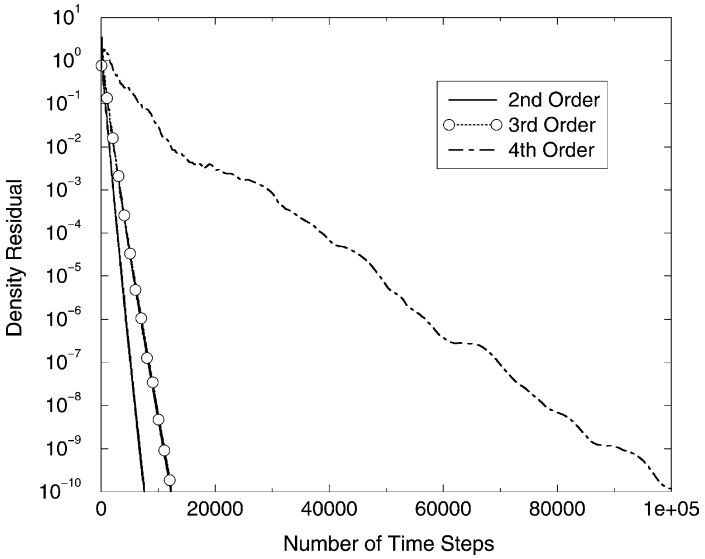

Fig. 14. Convergence histories on the medium 32×8 mesh for different SV schemes.

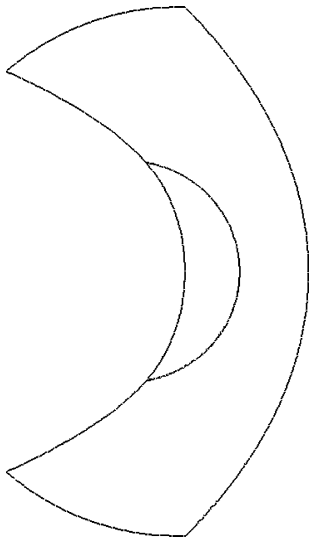

Fig. 15. Sonic line for the Ringleb's flow problem.

on an I1B2 SV. The same grids were employed in the simulations, and the computational results indeed were dramatically improved. Shown in Fig. 13 are the computed Mach contours, and the entropy errors are presented in Table 3. Note that the artificial wake present in the Mach contours computed with the I1B1 SV completely disappeared. A symmetric flow pattern was attained with grid refinement. The entropy errors generated on each grid with the same number of DOFs are also smaller than those computed with a second-order FV scheme. This case shows that a higher than linear boundary representation is important for all the SVs including the linear SV.

Finally convergence histories with I1B2, I2B2 and I3B3 SVs on the medium 32×8 grid are displayed in Fig. 14

4.2. Ringleb flow problem

This flow is a smooth analytical solution of the Euler equations derived with the so-called "hodograph transformation" [5]. The flow depends on the inverse of the stream function κ and the velocity magnitude q. In the present computation, we choose the values $\kappa = 0.7$ and $\kappa = 1.2$ to define the solid walls, and $q = 0.5$ to define the inlet and outlet boundaries. This flow problem is a much more difficult case than the subsonic

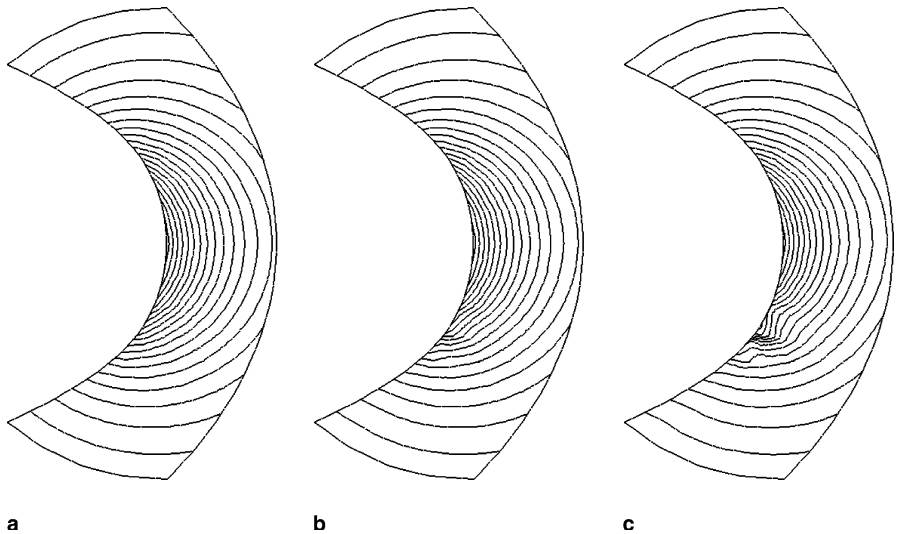

Fig. 18. Mach number contours computed using the I2B2 SV on the coarsest mesh at different time steps showing the development of a shock wave in the flow field. (a) $n = 1200$. (b) $n = 4200$. (c) $n = 7200$.

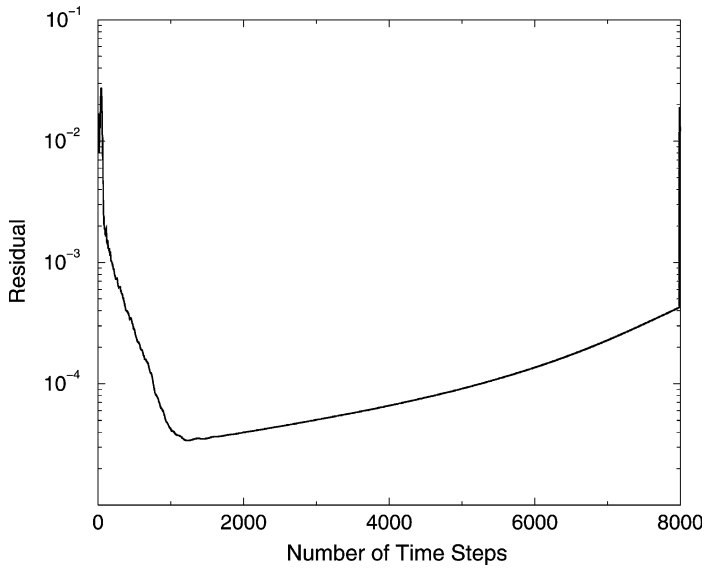

Fig. 19. Convergence history for the Ringleb problem using I2B2 SV on the coarsest mesh.

flow around a circular cylinder because the flow is transonic, and reaches a maximum Mach number of 1.42. Physically Ringleb flow represents a shockless transonic flow around a symmetric blunt obstacle, and is irrotational and isentropic. The flow reaches supersonic speed close to the nose of the blunt body. The sonic line for the problem is displayed in Fig. 15. Note that there is a large supersonic region in this flow. This case was more challenging than the authors originally anticipated because low order schemes tend to generate shocks in the simulation process, and the shock waves can quickly drive the simulation to divergence if no limiters are employed.

We again employed four different computational grids to perform an accuracy study. These grids are the triangulations of four structured grids of 16×4, 32×8, 64×16 and 128×32 cells, which are shown in Fig. 16.

Computations were then carried out using I1B1, I2B2 and I3B3 SVs on all the computational grids. Since the analytical solution is smooth, no limiters were employed in the numerical simulation. With the I1B1 SV, a shock wave quickly developed in the numerical solutions on all the grids, eventually making the simulation divergent. A typical solution computed with the I1B1 SV is shown in Fig. 17, which displays the Mach contours after a shock wave was developed in the numerical solution. Note that the linear bound-

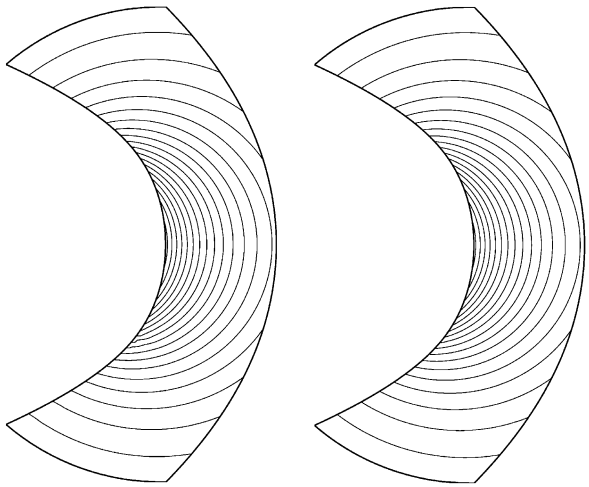

Fig. 20. Mach number contours computed with I2B2 spectral volumes. (a) 64×16 mesh. (b) 128×32 mesh.

Table 4
Accuracy study of SV schemes with the Ringleb flow

Order of interpolation	Grid	L_∞ error	L_∞ order	L_1 error	L_1 order
I2B2 (nq = 2)	$16 \times 4 \times 2$	Diverged	–	Diverged	–
	$32 \times 8 \times 2$	Diverged	–	Diverged	–
	$64 \times 16 \times 2$	3.98e − 4	–	2.82e − 6	–
	$128 \times 32 \times 2$	3.95e − 5	3.33	4.61e − 7	2.63
I3B3 (nq = 2)	$16 \times 4 \times 2$	5.82e − 4	–	2.01e − 5	–
	$32 \times 8 \times 2$	4.55e − 5	3.68	2.17e − 6	3.21
	$64 \times 16 \times 2$	7.37e − 6	2.63	2.70e − 7	3.01
	$128 \times 32 \times 2$	7.93e − 7	3.22	2.41e − 8	3.49

ary representation produced large errors near the solid boundaries. With the third-order I2B2 SV, the simulations on the two coarsest meshes still diverged. To investigate why the simulation diverged, the intermediate solutions on the coarsest mesh using the I2B2 SV are displayed in Fig. 18. The flow field was initialized with the analytical solution. The convergence history for this case is displayed in Fig. 19. Note that the simulation was converging monotonically until time step of about 1200, when the residual reached a minimum value. The Mach contours at this time step look very reasonable and is obviously shockless, as shown in Fig. 18(a). After that, the residual started to increase and eventually the simulation diverged. The solutions at time steps of 4200 and 7200 are displayed in Fig. 18(b) and (c). Clearly the divergence was caused by the shock wave formed in the flow field. It is conjectured that small numerical errors induced

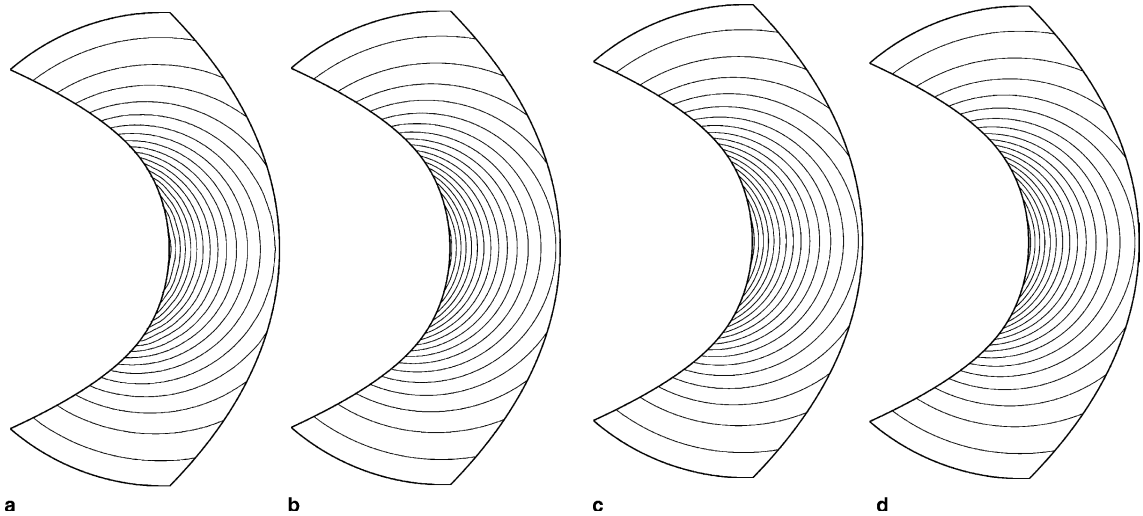

Fig. 21. Mach number contours computed with I3B3 spectral volumes. (a) $16 \times 4 \times 2$ mesh. (b) $32 \times 8 \times 2$ mesh. (c) $64 \times 16 \times 2$ mesh. (d) $128 \times 32 \times 2$ mesh.

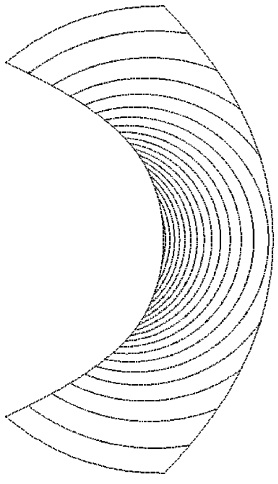

Fig. 22. Mach number contours computed with I1B2 spectral volumes on the finest mesh.

the generation of a shock wave in the flow field, which drove the simulation to divergence. On the two finer meshes, the I2B2 SV was capable of producing converged smooth shockless flow. The computed Mach contours are shown in Fig. 20. The entropy errors are presented in Table 4.

All simulations using the fourth-order I3B3 SV are convergent, and shockless solutions were successfully computed as shown in Fig. 21, which displays the Mach contours. The entropy errors for the I3B3 SV are again presented in Table 4. High-order accuracy is shown for both the I2B2 and I3B3 SVs. A convergent solution using an I1B2 SV was obtained on the finest mesh. The Mach contours are displayed in Fig. 22. Note the dramatic difference between the contours shown in Fig. 17 and 22.

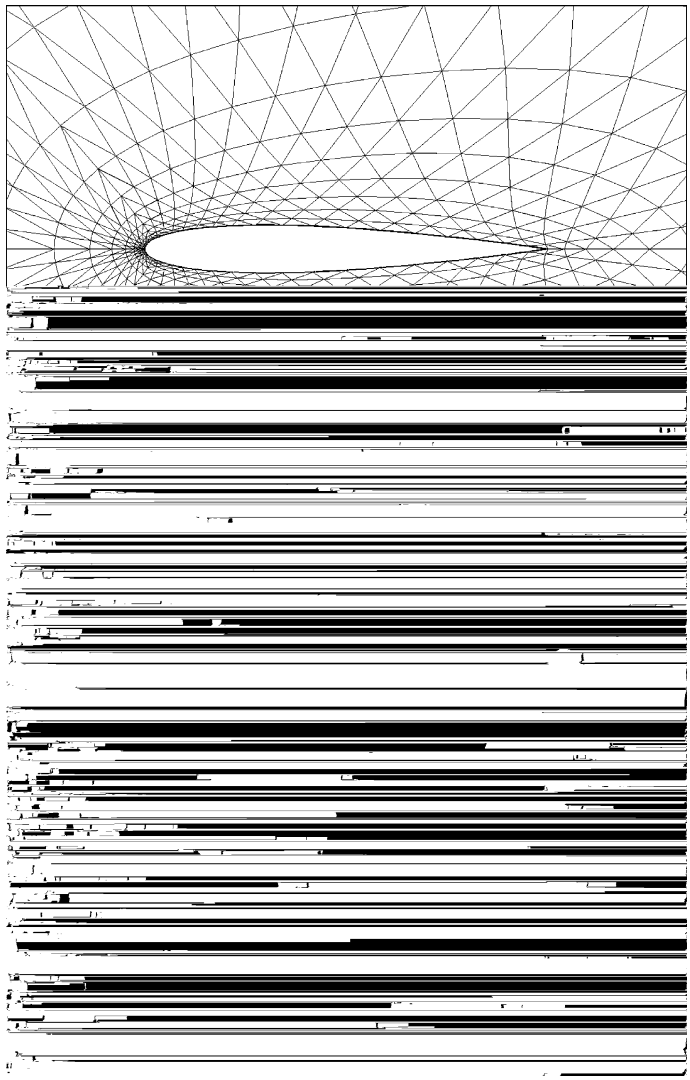

Fig. 23. The computational grids for a fourth-order SV scheme and second-order FV scheme. (a) SV mesh $(48 \times 16 \times 2)$. (b) FV mesh $192 \times 64 \times 2$.

4.3. Subsonic flow over a NACA0012 airfoil

As a final demonstration for a more realistic geometry, subsonic flow around a NACA0012 airfoil at Mach = 0.4, and angle of attack of 5 degrees is simulated. In this simulation, the computational results using the fourth-order SV scheme on a very coarse mesh with $48 \times 16 \times 2$ triangles are compared with those using a second-order MUSCL type FV method on a twice finer mesh with $192 \times 64 \times 2$ triangles. Therefore the number of DOFs in the FV simulation is 24,576 while it is 15,360 in the SV simulation. Again the entropy production in the solution is used as the indicator for the solution accuracy. For the fourth-order SV scheme, the boundary is approximated with 48 piece-wise cubic segments. For the second-order FV scheme, the airfoil surface is approximated with 192 linear segments. The computational meshes used for both the SV and FV methods are displayed in Fig. 23. The outer boundary is 20 chords away from the center of the airfoil. The pressure and Mach contours computed with both the SV and FV schemes are plotted together in Figs. 24 and 25. Note that the agreement is very good (the disagreement shown is mainly due to plotting errors on the coarse SV grid). The average entropy error with the second-order FV method is $1.04e-5$, while the average entropy error with the fourth-order SV scheme is $3.28e-6$, which is more than a factor of 3 smaller. The entropy errors along the airfoil surface are plotted for both computational results in Fig. 26. Note that although the second-order FV scheme used a much finer grid, the solution quality of the fourth-order SV scheme is superior. The convergence histories for both simulations are displayed in Fig.

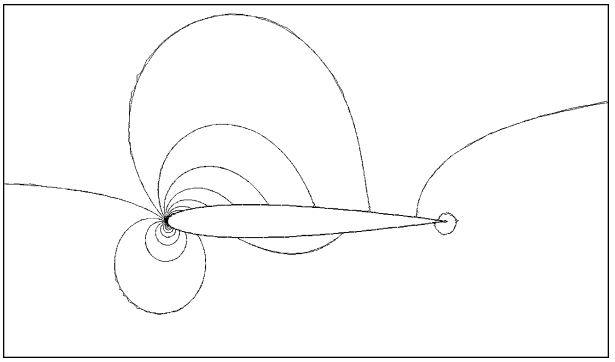

Fig. 24. Computed pressure contours using both a fourth-order SV scheme and a second-order FV scheme.

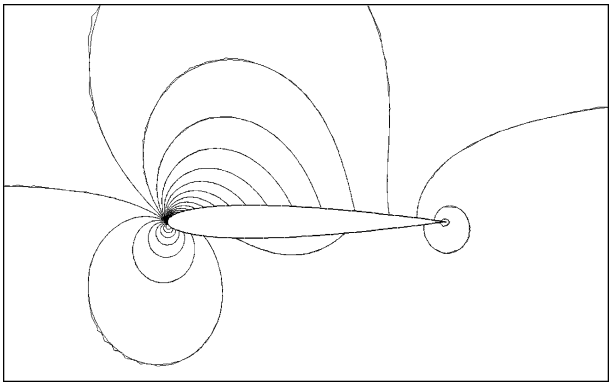

Fig. 25. Computed Mach contours using both a fourth-order SV scheme and a second-order FV scheme.

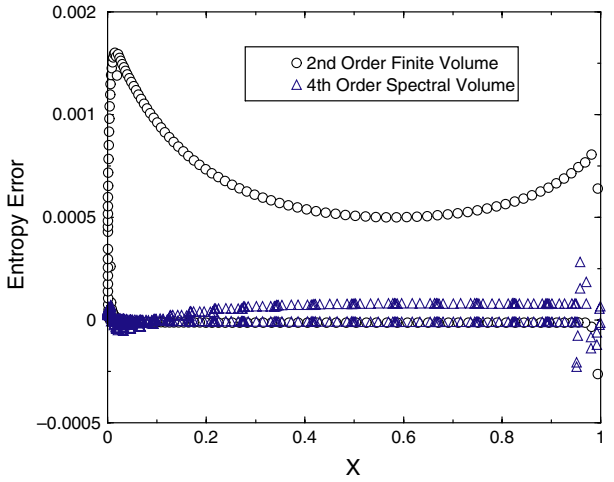

Fig. 26. Comparison of entropy errors along the airfoil surface.

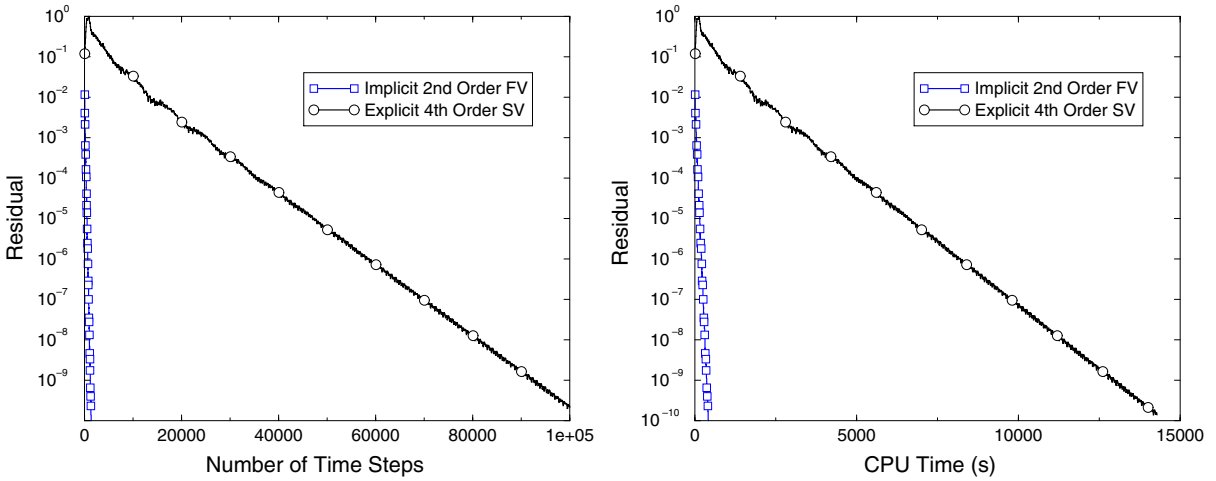

Fig. 27. Comparison of convergence histories between the implicit second-order FV method and the explicit fourth-order SV method.

27. In the FV simulation, an implicit block lower-upper symmetric Gauss–Seidel approach was used [4], resulting in much faster convergence. In this case, it took about 410 s for the implicit FV method to converge, while it took 14,000 s for the explicit SV scheme to converge. This plot also clearly demonstrates the need to develop efficient implicit solution algorithms for the high-order methods, in order to reap their potential benefits.

5. Conclusions

The spectral volume method has been successfully extended to 2D Euler equations with high-order boundary representation through the use of more general spectral volumes with curved edges. A uniform

free stream is preserved with the present implementation. Since in most cases, a spectral volume has at most one curved edge, simplified curved spectral volumes were developed and used in this study. This treatment significantly simplifies the numerical implementation and has been shown to work well. Three representative inviscid cases were used to test the curved SVs. It has been found that nearly optimum order of accuracy can be obtained in the L_1 norm with respect to entropy errors, while an order reduction in accuracy was observed in the L_∞ norm. Comparisons were also made between high-order SV schemes and a second-order finite volume method. It was shown that a fourth-order SV scheme produced a much more accurate numerical solution on a much coarser mesh than a second-order FV scheme for the case of subsonic flow around a NACA0012 airfoil. However, more efficient solution algorithms are urgently needed to reap the benefit of high-order methods. Linear boundary representation was also used with third- and fourth-order SV schemes for the case of subsonic flow over a cylinder, and we were unable to obtain convergent numerical solutions. In fact, it appears that higher than linear boundary representations are required in SV schemes of any order to produce acceptable results. For the Ringleb flow problem, it has been found high-order schemes with enough grid resolution are necessary to reproduce the smooth shockless transonic flow.

Acknowledgements

The authors thank Dr. H.T. Huynh of NASA Glenn Research Center for sharing his program for the Ringleb flow problem.

References

[1] R. Abgrall, On essentially non-oscillatory schemes on unstructured meshes: analysis and implementation, J. Comput. Phys. 114 (1994) 45–58.
[2] T.J. Barth, P.O. Frederickson, High-order solution of the Euler equations on unstructured grids using quadratic reconstruction,'' AIAA Paper No. 90-0013, 1990.
[3] F. Bassi, S. Rebay, High-order accurate discontinuous finite element solution of the 2D Euler equations, J. Comput. Phys. 138 (1997) 251–285.
[4] R.F. Chen, Z.J. Wang, Fast, block lower-upper symmetric Gauss Seidel scheme for arbitrary grids, AIAA J. 38 (2000) 2238.
[5] G. Chiocchia, Exact solutions to transonic and supersonic flows. Technical Report AR-211, AGARD, 1985.
[6] B. Cockburn, C.-W. Shu, TVB Runge-Kutta local projection discontinuous Galerkin finite element method for conservation laws II: general framework, Math. Comput. 52 (1989) 411–435.
[7] B. Cockburn, C.-W. Shu, The Runge-Kutta discontinuous Garlerkin method for conservation laws V: multidimensional systems, J. Comput. Phys. 141 (1998) 199–224.
[8] S.K. Godunov, A finite-difference method for the numerical computation of discontinuous solutions of the equations of fluid dynamics, Mat. Sb. 47 (1959) 271.
[9] A. Harten, B. Engquist, S. Osher, S. Chakravarthy, Uniformly high order essentially non-oscillatory schemes III, J. Comput. Phys. 71 (1987) 231.
[10] C. Hu, C.-W. Shu, Weighted essentially non-oscillatory schemes on triangular meshes, J. Comput. Phys. 150 (1999) 97–127.
[11] Y. Liu, M. Vinokur, Z.J. Wang, Three-dimensional high-order spectral finite volume method for unstructured grids, in Proceedings of 16th AIAA CFD Conference, Orlando, Florida, 2003, also AIAA Paper No. 2003-3837.
[12] P.L. Roe, Approximate Riemann solvers, parameter vectors, and difference schemes, J. Comput. Phys. 43 (1981) 357–372.
[13] C.-W. Shu, Total-Variation-Diminishing time discretizations, SIAM J. Sci. Stat. Comput. 9 (1988) 1073–1084.
[14] B. van Leer, Towards the ultimate conservative difference scheme V. A second order sequel to Godunov's method, J. Comput. Phys. 32 (1979) 101–136.
[15] Z.J. Wang, A fast nested multi-grid viscous flow solver for adaptive Cartesian/quad grids, Int. J. Numer. Meth. Fluids 33 (2000) 657–680.
[16] Z.J. Wang, Spectral (finite) volume method for conservation laws on unstructured grids: basic formulation, J. Comput. Phys. 178 (2002) 210.

[17] Z.J. Wang, Y. Liu, Spectral (finite) volume method for conservation laws on unstructured grids II: extension to two-dimensional scalar equation, J. Comput. Phys. 179 (2002) 665.
[18] Z.J. Wang, Y. Liu, Spectral (finite) volume method for conservation laws on unstructured grids III: extension to one-dimensional systems, J. Sci. Comput. 20 (2004) 137.
[19] Z.J. Wang, L. Zhang, Y. Liu, Spectral (finite) volume method for conservation laws on unstructured grids IV: extension to two-dimensional Euler equations, J. Comput. Phys. 194 (2004) 716.
[20] O.C. Zienkiewicz, R.L. Taylor, The Finite Element MethodThe Basics, vol. 1, Butterworth–Heinemann, Oxford, England, 2000.